



Cite this: *Mater. Adv.*, 2022,
3, 3631

Multifunctional sandwich-structured double-carbon-layer modified SnS nanotubes with high capacity and stability for Li-ion batteries†

Jia Luo, Huaiyu Li, Guo Yu, Wenyuan Xu, Hong Yin * and Zhaohui Hou *

Tin monosulfide (SnS) anodes have attracted much attention for lithium-ion batteries (LIBs) due to their excellent chemical stability, high theoretical specific capacity and outstanding reversibility. However, the slow kinetics and large volume expansion of intrinsic SnS electrodes in the conversion reaction process restrict their application to a certain extent. To address the poor conductivity and volume fluctuation, N-doped double-carbon-layer protective hierarchical structures decorating SnS nanotubes (N-DCSNs) are introduced by *in situ* polymerization directed using a g-C₃N₄ soft template. Particularly, N-doped double carbon layers provide fast transport channels for electrons and ions, affording decent conductivity and rapid ionic diffusion rate. Most importantly, the volume expansion of SnS during the charge–discharge cycles can be buffered owing to the confinement effect of the double carbon layer. Synergistic effects of N-DCSNs enhance the mechanical integrity and electrochemical kinetics during the charge–discharge process, leading to high-capacity retention and long-term stability properties. As a remarkable anode for LIBs, the N-DCSN electrode delivers high capacities of 911.5 and 511.3 mA h g^{−1} at 0.2 and 1.0 A g^{−1} after 270 and 1000 cycles, respectively. The feasible and versatile structure design can offer new ideas for the preparation and regulation of other transition metal sulfide anode materials, and provide a relevant experimental basis for the further development of lithium/sodium storage equipment.

Received 6th January 2022,
Accepted 14th March 2022

DOI: 10.1039/d2ma00017b

rsc.li/materials-advances

1. Introduction

The demand for clean energy storage equipment is increasing due to the intensification of the energy crisis and rapid economic development. As secondary rechargeable batteries, lithium-ion batteries (LIBs) have attracted much attention in recent years because of their high energy density, wide working voltage range, long service life and environmental friendliness.^{1–3} Moreover, LIBs have been widely used in electric vehicles, portable devices, power grid energy storage and other fields.⁴ However, currently as a commercial LIBs anode material, graphite carbon has many disadvantages, such as low charge and discharge plateau, side reactions, poor rate performance, and the specific capacity being close to the theoretical capacity threshold.^{5,6} Therefore, it is important to find a more suitable anode material for LIBs.

Among various anode materials, metal chalcogenides based on conversion/alloying reactions are attractive because of their

high theoretical specific capacity, outstanding chemical stability and eminent reversibility. In particular, as the voltage lag of metal sulfide is smaller than that of metal oxide, which makes the metal sulfide show higher energy efficiency for LIBs.⁷ A promising basal material for storing various alkali metal ions through the conversion/alloying reaction is tin monosulfide (SnS) with a unique two-dimensional layered structure.⁸ The layered structure provides abundant reaction sites for charge storage, which is conducive to e[−]/Li⁺ transport and electrolyte diffusion. The effect can improve the ion intercalation efficiency, which shows high theoretical specific capacity (782 mA h g^{−1}), and has broad electrochemical application prospects in power storage devices.⁹ However, the complex lithium storage mechanism of SnS is based on the conversion reaction to form Li₂S and Sn. The alloying reaction occurs at the same time to form a Li_xSnS alloy leading to some serious problems.¹⁰ First, a redox reaction will occur in the process of lithiation/delithiation to form multi-phase structures, which will lead to slow kinetic problems. Second, the inherent electronic conductivity of SnS is poor, which will directly affect the rate performance of LIBs. Third, irrespective of whether a conversion reaction or an alloying reaction occurs, SnS will produce large volume strain in the electrochemical process, including electrode particle pulverization, deterioration or agglomeration, resulting in poor cycle performance.¹¹

Key Laboratory of Hunan Province for Advanced Carbon-based Functional Materials, Hunan Institute of Science and Technology, Yueyang 414006, China.
E-mail: 2017507027@hust.edu.cn, zhaohuihou@126.com

† Electronic supplementary information (ESI) available. See DOI: 10.1039/d2ma00017b

Relevant approaches are adopted to address these problems, such as combining with carbon materials,^{12–15} preparing nano hollow structures,⁷ doping and modification of heteroatoms.^{16–18} Carbon materials can play an important role in buffering volume change, enhancing ion and electron transport and reducing the size of anode materials by constructing a reasonable structure.¹⁹ Hollow nanostructures can not only inhibit metal agglomeration, but also expose more active sites to ensure the full use of electroactive materials. Additionally, nitrogen doping can also increase the electrochemical reactivity, conductivity and surface wettability of carbon, which is conducive to the diffusion of Li-ion through the interface between the carbon electrode and electrolyte.²⁰ Jin *et al.* prepared N-doped carbon-coated SnS nanoparticles, which delivered a capacity of 741.4 mA h g⁻¹ at 100 mA g⁻¹ current density after 200 cycles, showing better cycling stability.⁷ Xia *et al.* prepared a SnS/C nanofiber membrane by a simple and general electrospinning method, which is directly used as an independent anode in LIBs, providing excellent electrochemical performance.¹⁶ However, few Sn-based anode materials have achieved a super-long cycle life of more than 500 cycles, which may be due to the fact that carbon has not been excavated well. In order to solve this problem, carbon matrix composite electrodes can be designed rationally by selecting a suitable carbon source. Due to the particularity of g-C₃N₄, it has been widely used in photocatalysis, electrocatalysis, supercapacitors and energy storage systems.^{21,22} The graphite phase C₃N₄ (g-C₃N₄) has a similar structure to graphene. It has a high specific surface area, easy synthesis, excellent chemical stability, environmental friendliness and high theoretical lithium storage capacity (524 mA h g⁻¹).²³ The g-C₃N₄ has been broadly applied for building soft templates or affording high-speed electronic channels to improve the Li-storage of metal sulfide. Yin *et al.* constructed nanoflower SnS₂ based on g-C₃N₄ nanosheet composite materials as efficient anode electrodes of LIBs.²⁴ It is worth noting that polyaniline (PANI) has the characteristics of high specific capacity, admirable redox reversibility, high conductivity, simple synthesis method, and low cost.²⁵ It is widely used in chemical power supply and can alleviate the problem of poor cycling stability of LIBs. Therefore, the reasonable design of the carbon composite material can obtain excellent performance of anode electrodes.

In this study, N-doped double-carbon-layer protective hierarchical structures decorating SnS nanotubes (N-DCSNs) are introduced for addressing the poor conductivity and volume fluctuation by hydrothermal and *in situ* polymerization. Based on the structure design, the N-doped double-carbon layer provides abundant active sites and defects that help shorten ion and electron transport paths. In addition, it helps to maintain the mechanical integrity of the structure and stabilize SEI formation to buffer volume changes of SnS. Structural advantages enhance mechanical integrity and electrochemical kinetics during the charge-discharge process, leading to long-term stable lithium storage performances. The N-DCSN electrodes deliver high capacities of 511.3 mA h g⁻¹ after 1000 cycles at 1.0 A g⁻¹, and the coulombic efficiency can reach 95.9% after

the first discharge cycle. This method can be extended to the preparation of other carbon-coated electrodes, aiming at improving the conductivity and structural stability of anode materials for LIBs.

2. Experimental section

2.1 Materials preparation

All reagents including stannous chloride dihydrate (SnCl₂·2H₂O, Xilong Chemical Co., Ltd, China), melamine (C₃H₆N₆, Sinopharm Chemical Reagent Co., Ltd, China), thioacetamide (TAA, C₂H₅NS, Sinopharm Chemical Reagent Co., Ltd, China), polyvinylpyrrolidone (PVP, (C₆H₉NO)_n, M_w = 58 000, Aladdin, China), Aniline (C₆H₇N, Aladdin, China), ammonium persulfate (H₈N₂O₈S₂, Aladdin, China), anhydrous ethanol (CH₃CH₂OH, Hunan Huihong Reagent Co., Ltd, China), and hydrochloric acid (HCl, Hunan Huihong Reagent Co., Ltd, China) are analytical grade and can be used directly without purification. The schematic of the fabrication process of N-DCSNs is shown in Fig. 1. In addition, bare SnS and g-C₃N₄ modified SnS composites (CN/SnS) were prepared to compare with N-DCSNs.

(1) Preparation of bare SnS: Firstly, 0.5 g PVP was dispersed in 60 ml absolute ethanol by ultrasound, then 0.45 g SnCl₂·2H₂O and 0.15 g TAA were added successively, and were stirred for 30 min. Then the mixed solution was placed in a hydrothermal kettle and reacted at 180 °C for 12 h to obtain pure SnS nano flower balls.

(2) Preparation of CN/SnS composites: Firstly, melamine was placed in a crucible and heated to 550 °C at 5 °C min in the air of a muffle furnace for 4 h. When the temperature was reduced to room temperature, it was ground into powder to obtain g-C₃N₄. 0.5 g PVP and 2 g g-C₃N₄ powder were dispersed in 60 ml absolute ethanol by ultrasound. Then 0.45 g SnCl₂·2H₂O and 0.15 g TAA were added successively and stirred for 4 h. Then, the dispersion was placed in a hydrothermal kettle and reacted at 180 °C for 12 h. Finally, it was centrifuged, washed with ethanol several times and dried to obtain CN/SnS composites.

(3) Preparation of N-DCSNs: The CN/SnS composites prepared above were ultrasonically dispersed in 50 ml deionized water, and 0.3 ml concentrated HCl was added for ultrasonic uniformity. 0.45 g aniline monomer was added in an ice bath and stirred for several minutes, then 1.23 g ammonium persulfate was added slowly and was stirred for 12 h. After that, it was centrifuged, washed with deionized water several times, and dried in a 70 °C vacuum oven overnight. Finally, in a tubular furnace, the temperature was raised to 800 °C at a rate of 5 °C min⁻¹ in Ar/H₂ gas, the temperature was maintained for 2 h, and then cooled to room temperature to obtain N-DCSNs.

2.2 Structure and morphology characterization

Scanning electron microscopy (SEM, HITACHI S-4800) and transmission electron microscopy (TEM, jeol2100f) were used to observe the micro morphology of the prepared materials; the crystal structure and defect characteristics of the prepared



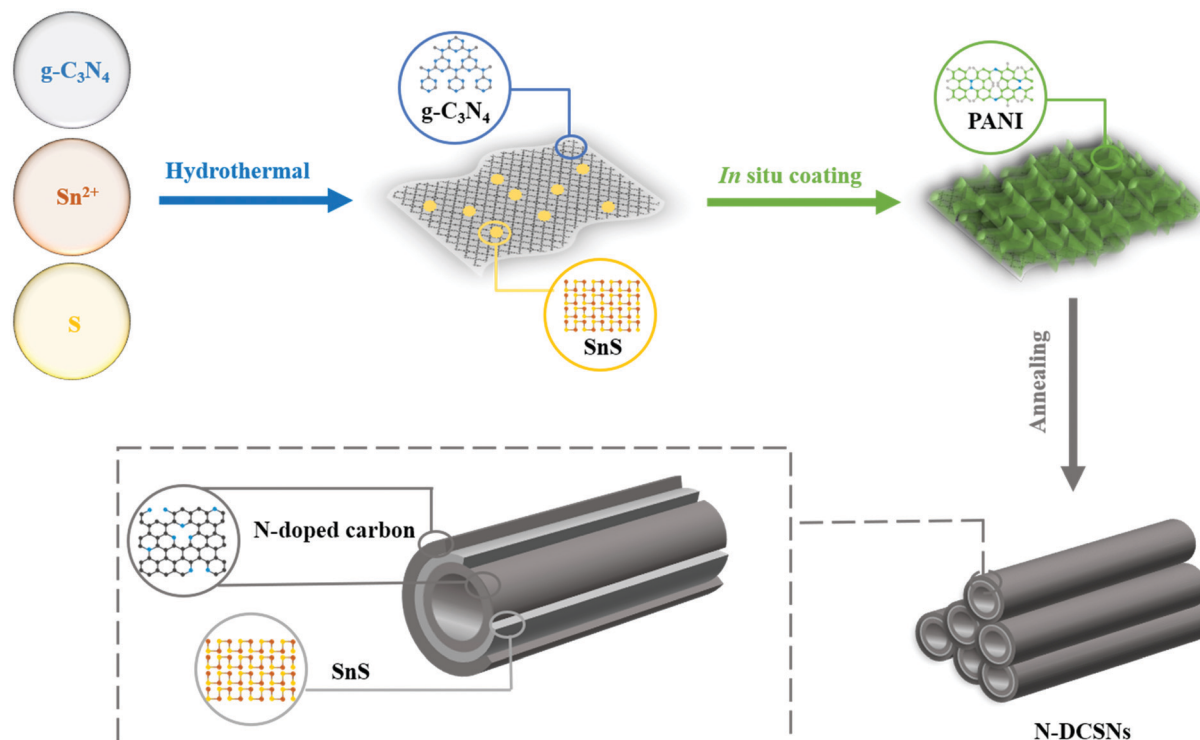


Fig. 1 Schematic illustration of the synthesis process for the N-DCSNs.

materials were characterized using an X-ray diffractometer (XRD, Rigaku, Ultima IV) and Raman spectrometer (HORIBA Scientific LabRAM HR Evolution); the surface chemical composition of the prepared materials was analyzed by X-ray photoelectron spectroscopy (XPS, Thermo Scientific K-Alpha); the specific surface area, pore volume and pore diameter of the material were measured by N₂ adsorption/desorption isotherm (BET, Mike 2460).

2.3 Electrochemical tests

(1) Preparation of working electrodes: Appropriate amounts of active materials, binder (PVDF) and conductive agent (Super P) were weighed respectively according to the mass ratio of 8 : 1 : 1, and were ground fully. The mixture was placed in a small 5 ml beaker, an appropriate amount of 1-methyl-2-pyrrolidone was added, and stirred at room temperature for 8 h to form a uniform slurry. The slurry was coated on copper foil, dried at 70 °C in a vacuum for 12 h, and cut into 12 mm diameter discs to obtain active material loaded working electrodes. The mass loading of the electrode is about 0.91 mg cm⁻² and the area of each electrode is 1.13 cm².

(2) Assembly of button batteries: The working electrodes were placed in the glove box protected by high-purity argon. The electrodes, diaphragms and lithium sheets were placed at the bottom shell of CR 2025 button batteries successively, an appropriate amount of electrolyte (1.0 M LiPF₆ in EC:DMC:EMC = 1 : 1 : 1 Vol% with 5.0% FEC) was injected. And the electrodes were packaged into coin half batteries for the electrochemical test.

(3) Electrochemical performance test: The CT2001A battery test system was used to test the cycle performance and rate performance of the batteries; the voltage range of the battery test was set to 0.01–3 V at 0.2 and 1.0 A g⁻¹, respectively. The electrochemical workstation (Interface 1010E) was used to test the cyclic voltammetry and AC impedance of the batteries. The sweep rate range of cyclic voltammetry was 0.2–1.0 mV s⁻¹.

3. Results and discussion

3.1 Characterization of N-DCSNs

XRD and Raman spectra are used to analyze the crystal structure of N-DCSNs. The XRD standard card can be indexed to the orthogonal SnS map (JCPDS No. 39-0354). Fig. 2a shows the XRD diagrams of bare SnS, CN/SnS composites and N-DCSNs, it can be clearly observed that the diffraction peaks of the three samples appear at theta degrees of 30.5°, 32° and 39°, corresponding to the (111), (040) and (131) peaks of SnS, respectively.¹⁶ In addition, except for pure SnS, diffraction peaks appear at theta degrees of 26.5° and 45°, corresponding to the (002) and (101) peaks of graphitized carbon, respectively.²⁶ The result indicates that the graphitization degree of N-DCSNs is relatively strong, which will be conducive to the cycling stability of LIBs. Fig. 2b displays the Raman spectrum of N-DCSNs. The Raman shift is the D peak belonging to the carbon defect site at 1350 cm⁻¹ and the G peak belonging to the graphitized carbon at 1580 cm⁻¹. The intensity ratio (*I_D*/*I_G*) of the D peak (disordered structure) to G peak (graphite structure) can reflect the degree of defects in carbon materials.²⁷



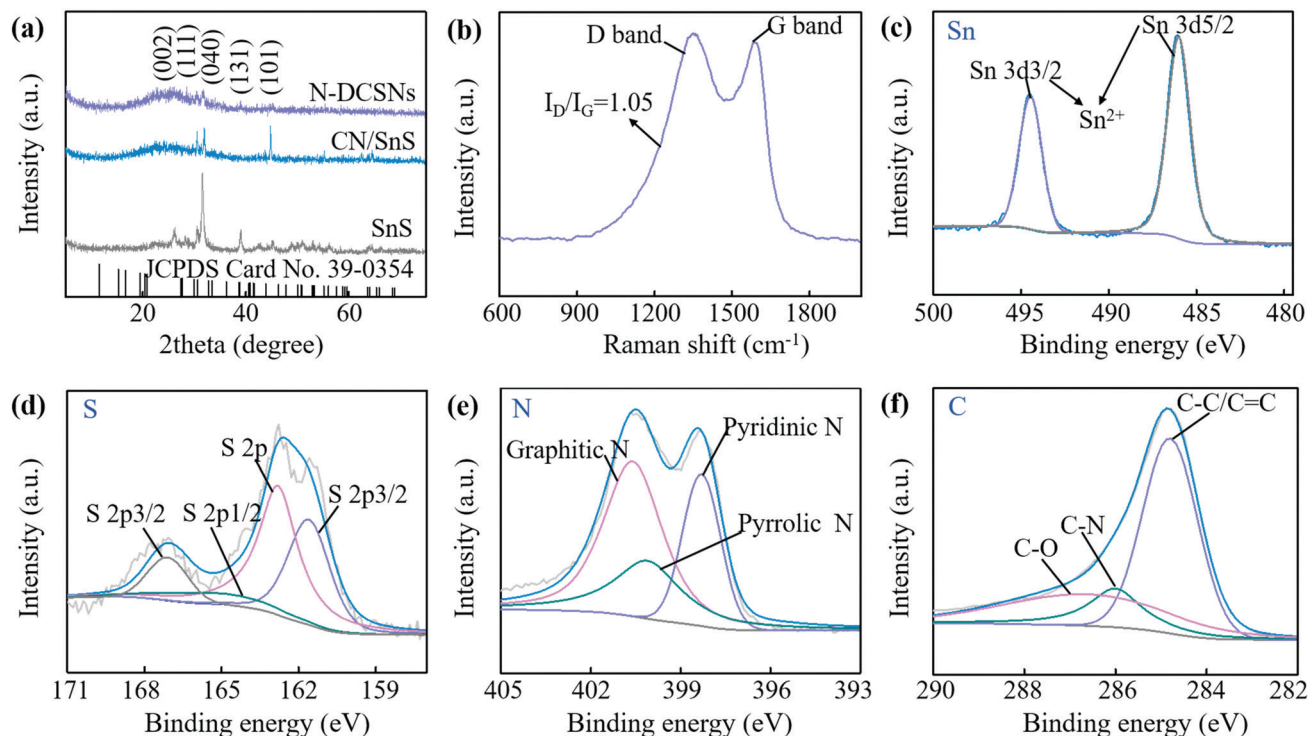


Fig. 2 (a) XRD patterns of bare SnS, CN/SnS composites and N-DCSNs. (b) Raman spectra of N-DCSNs. (c–f) XPS spectra of N-DCSNs for (c) Sn 3d, (d) S 2p, (e) N 1s, and (f) C 1s.

The I_D/I_G is about 1.05 of the N-DCSN sample, which proves that N-DCSNs have highly disordered properties. The pore size distribution curve and nitrogen isothermal adsorption–desorption curve of N-DCSNs are displayed in the ESI† (Fig. S1). Fig. S1a (ESI†) reveals that the pore diameter of N-DCSNs is mainly concentrated in the range of 2–4 nm, indicating that N-DCSNs have a mesoporous structure. Fig. S1b (ESI†) shows that there is an H2 type hysteresis loop at P/P_0 of 0.5–0.9 in the N_2 isothermal adsorption–desorption curve of N-DCSNs, which is a type IV isotherm, mainly due to the pore connectivity effect.

In order to determine the carbon content and elemental composition of N-DCSNs, thermogravimetric analysis and XPS measurement are carried out. The TGA curve is shown in Fig. S2 (ESI†). The main weight loss temperature range is 400–600 °C, which can be attributed to the conversion from SnS to SnO_2 and the gasification of carbon materials.²⁸ Since the relative molecular weights of SnS and SnO_2 are equal, the carbon content in the composite can be determined to be about 64.68%.^{15,29} In particular, the carbon materials could contribute some capacities as the active material.³⁰ Fig. 2c–f exhibit the XPS measurement spectra of Sn, S, N and C of N-DCSNs, and the full spectrum is shown in the ESI† (Fig. S3). Fig. 2c manifests that the high-resolution Sn 3d spectrum can be deconvoluted into two main peaks. The two peaks at 494.5 and 486 eV can correspond to Sn 3d_{3/2} and Sn 3d_{5/2} of Sn^{2+} in SnS, respectively.³¹ The S 2p spectrum can be divided into four main peaks (Fig. 2d), and the peak at 161.6 eV can be attributed to S 2p_{3/2} of SnS.³² Two peaks at 162.8 and 165.25 eV conform to the C–S–C heterocyclic configuration,³³ and the weak peak at

167.1 eV is usually attributed to sulfate groups (C–SO_x–C).³⁴ These C–S–C bonds are rich in electron pairs, which is highly beneficial for improving the electrochemical reaction kinetics of SnS.¹⁶ The high-resolution N 1s spectrum in Fig. 2e shows that there are three peaks at 398.3, 400.1 and 400.6 eV, representing the pyridinic N, pyrrolic N and graphitic N, respectively.³⁵ As shown in Fig. 2f, the main peak of the C 1s spectrum at 284.3 eV is attributed to the C–C/C=C bond, while the small peaks at 286 and 286.6 eV are attributed to the C–N bond and C–O bond, respectively.³⁶ The results indicate that nitrogen atoms are successfully doped at the edge or defect position of the carbonized PANI lattice. N-doped carbon can improve the reactivity and electronic conductivity by producing extrinsic defects.³⁷ Initially, nitrogen doped carbon matrix can effectively reduce the energy barrier of lithiation and promote the rapid diffusion of Li^+ and e^- on the surface and inside of N-DCSN composites. Moreover, the introduction of pyridinic nitrogen and pyrrolic nitrogen can produce a large number of pores and surface defects on the carbon matrix, expose more active sites, and provide a shorter diffusion path for Li^+ insertion.³⁸ Therefore, N-doped carbon matrix coated SnS particles can enhance the lithium storage capacity and improve the electrochemical performance of LIBs.

In order to further explore the structure and morphology of N-DCSNs, the morphological characteristics of bare SnS, CN/SnS composites and N-DCSNs are characterized by SEM. The result of N-DCSNs is shown in Fig. 3a while the morphology of bare SnS and CN/SnS composites is displayed in the ESI† (Fig. S4). According to SEM, the N-DCSN composite

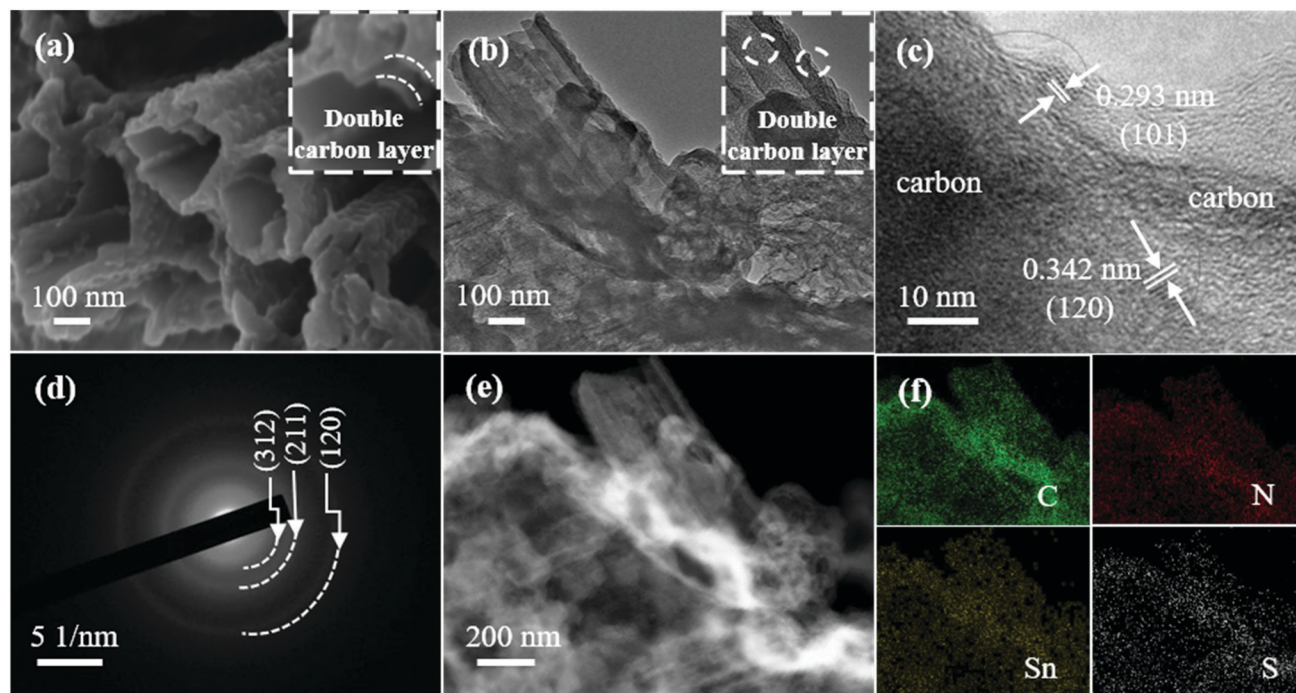


Fig. 3 (a) SEM and (b) TEM images of N-DCSNs. (c) The HRTEM image of SnS nanocrystals with typical lattice distances. (d) The ED pattern of N-DCSNs. (e and f) HAADF-STEM images with the corresponding elemental distribution images of N-DCSNs.

presents the morphology of sandwich double carbon layer coated SnS nanotubes. The amount of exposed tubular structure of N-DCSNs is less than that of CN/SnS composites, which may be due to the partial tubular morphology covered by the PANI carbonization layer. However, the addition of the second carbon layer of PANI can well alleviate the volume expansion of SnS in the lithiation/delithiation process. Moreover, the PANI carbonization skeleton helps maintain the mechanical integrity of the structure, enrich the charge transfer channels, provide more lithium storage active sites, shorten the transmission path of ions and electrons, and accelerate the diffusion rate of Li-ions.²⁵ By observing the TEM diagram of N-DCSNs (Fig. 3b), the double-layer carbon structure can be clearly seen in the sample, which matches the SEM image (Fig. 3a). The high resolution TEM (HRTEM) image (Fig. 3c) reveals clear lattice fringes with spaces of 0.293 nm and 0.342 nm, corresponding to the (101) and (120) planes of orthorhombic SnS, respectively.¹⁶ The selected area electron diffraction (SAED) pattern shown in Fig. 3d further confirms the existence of SnS, and different diffraction rings can be well matched to the (312), (211) and (120) planes of orthogonal SnS (JCPDS No. 39-0354).³⁸ The EDX elemental maps (Fig. 3e–g) illustrate that C, N, Sn and S elements are evenly distributed in the composite.

3.2 Lithium storage performance

The CV curve of the N-DCSN electrode is exhibited in Fig. 4a. The scanning voltage range is 0.005–3 V and the scanning rate is 0.5 mV s^{−1}. The reduction peak of about 1.11 V in the first cathode scan corresponds to the conversion reaction of SnS (SnS + 2Li⁺ + 2e[−] → Sn + Li₂S).²⁸ In subsequent cycles, the

cathode peak associated with the conversion reaction moved to about 1.30 V. Besides, the distinct cathodic/anodic peaks almost overlap after the second cycle, indicating reversible Li-ion storage attributed to the contribution of double carbon materials.^{12,15} The reduction peak value of 0.54 V is attributed to the irreversible decomposition of the electrolyte, resulting in the formation of a solid electrolyte interface (SEI), which is the main factor causing the irreversible capacity. The reduction peak value of about 0.3 V is related to the alloy reaction of metal Sn.³⁹ In anodic scanning, the oxidation peaks of 0.52 V and 0.68 V correspond to multi-step dealloying reaction, and the oxidation peak at 1.99 V may come from the reversible conversion reaction of SnS.^{40,41} At different scanning speeds, the CV curves of N-DCSN electrodes (Fig. S6a, ESI†) overlap well, indicating that N-DCSN electrodes have superior rate performance. These results are further verified by the constant current charge/discharge curve (Fig. 4b). The charge and discharge curves almost coincide even after 200 cycles, which shows that N-DCSN electrodes have high reversibility and capacity retention. The rate performance of the N-DCSN electrode is displayed in Fig. 4c. The reversible capacities of the N-DCSN composite are 980.1, 858.4, 782.1, 746 and 705.4 mA h g^{−1} at 0.1, 0.2, 0.5, 1.0 and 2.0 A g^{−1}, respectively. When the current density returned to 0.1 A g^{−1}, the discharge specific capacity quickly recovered to 781.5 mA h g^{−1}. It shows that the N-DCSN electrode has excellent rate performance, and its structure is not seriously damaged in the rapid charge and discharge process.⁴²

Cyclic performance is an important factor for measuring the electrochemical performance of materials. The cycling properties of bare SnS, CN/SnS composites and N-DCSNs as anode



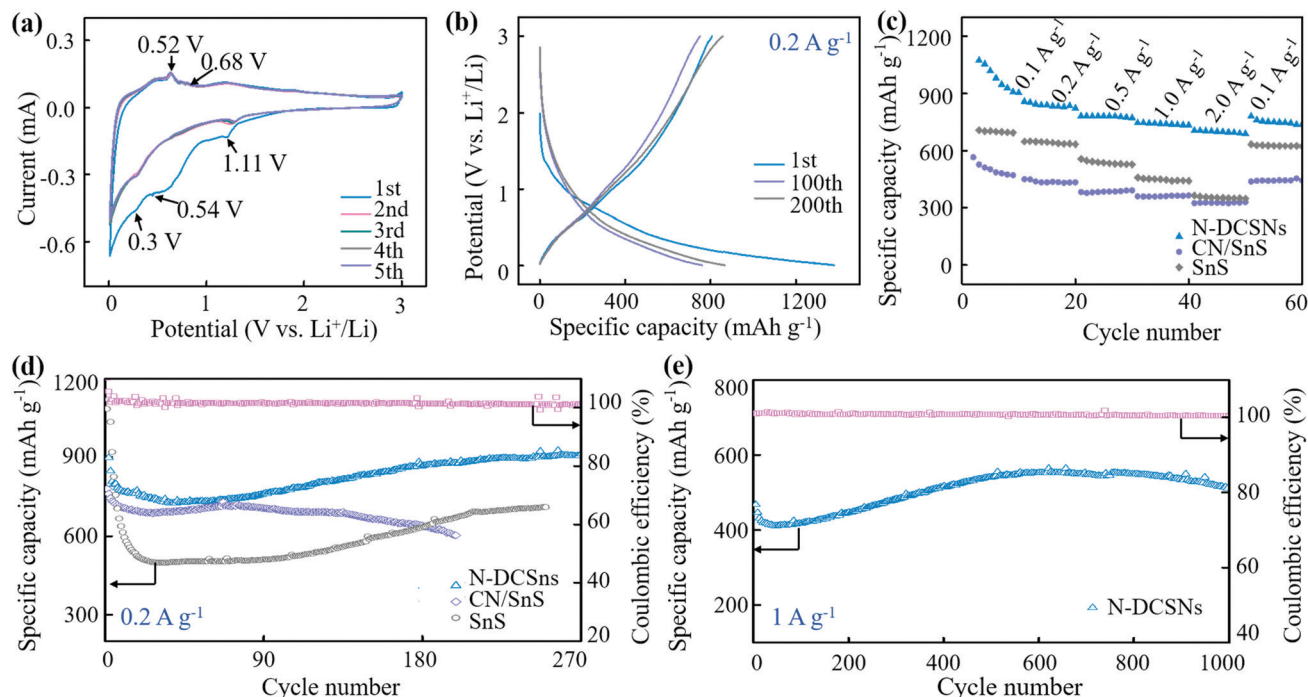


Fig. 4 (a) Cyclic voltammetry curves of N-DCSN electrodes between 0.01 and 3.0 V with a scan rate of 0.5 mV s^{-1} . (b) Constant current charge/discharge curve of N-DCSN electrodes at a rate of 0.2 A g^{-1} . (c) Rate performance of bare SnS, CN/SnS and N-DCSN electrodes at various current densities from 0.1 to 2.0 A g^{-1} . (d) Cycling performance of bare SnS, CN/SnS and N-DCSN electrodes at a current density of 0.2 A g^{-1} . (e) Long-term cycling performance of N-DCSN electrodes at a current density of 1.0 A g^{-1} .

materials for LIBs are tested at a current density of 0.2 A g^{-1} (Fig. 4d). The initial discharge specific capacity of the N-DCSN electrode can reach $1394.8 \text{ mA h g}^{-1}$. Due to the formation of a SEI film, irreversible capacity is inevitably generated.⁴³ In the subsequent cycle, the N-DCSN electrode decays slightly. At 44 cycles, the specific discharge capacity decreased to $727.6 \text{ mA h g}^{-1}$. However, in the overall charge–discharge process, the coulombic efficiency is maintained above 100%. The high coulombic efficiency can be attributed to the high conductivity of the PANI carbonized layer and the structural defects produced by the $\text{g-C}_3\text{N}_4$ soft template, which synergistically accelerates the electron and ion diffusion rates. Interestingly, with the increase of the number of cycles, the discharge specific capacity even shows an upward trend. The as-prepared electrode can deliver a specific discharge capacity of $911.5 \text{ mA h g}^{-1}$ at 0.2 A g^{-1} after 270 cycles. The increase of the specific discharge capacity may be attributed to the fact that the electrochemical grinding effect reduces the particle size of SnS nanoparticles in the continuous reaction. And the ultra-fine nanoparticles can effectively slow down the volume expansion, resulting in a higher reversible lithium storage capacity. In addition, the electrolyte will form a gel-like layer in the reaction process, which is also conducive to the increase of specific capacity.⁴⁴ Compared with the N-DCSN electrode, the initial discharge specific capacity of the bare SnS electrode also reached $1084.7 \text{ mA h g}^{-1}$ at 0.2 A g^{-1} . However, due to the large volume effect in the process of charge and discharge, the attenuation range of the discharge specific capacity becomes larger with the

increase of the number of cycles. The initial specific capacity of the CN/SnS electrode is only $779.4 \text{ mA h g}^{-1}$, and the overall attenuation of specific capacity during charge and discharge is not as large as that of the bare SnS electrode, but it is still less stable than that of the N-DCSN electrode.

The long cycling stability of the N-DCSNs electrode is further reflected in Fig. 4e. The N-DCSN electrode also showed capacity attenuation after the first cycle at a high current density of 1.0 A g^{-1} . However, with the increase in the number of subsequent cycles, the specific discharge capacity also tends to become stable. The discharge specific capacity of the N-DCSN electrode is still $511.3 \text{ mA h g}^{-1}$ after 1000 cycles, which proves that the N-DCSN electrode has excellent cycling stability and capacity retention. The excellent electrochemical properties of N-DCSN electrodes can be ascribed to the structural advantages of the materials. SnS nanoparticles were evenly embedded into the $\text{g-C}_3\text{N}_4$ soft template. The $\text{g-C}_3\text{N}_4$ is cracked at high temperatures to produce a porous structure and increase the specific surface area of the material. The special structure helps shorten the Li^+ and e^- transport paths, and provides abundant active sites. N-doped carbon matrix has high conductivity, which speeds up the reaction kinetic rate of N-DCSN electrodes. Generally, if nanoparticles are exposed to electrolytes in a large area, too many side reactions will occur, resulting in the reduction of coulombic efficiency. Besides, the carbon layer is relatively fragile, and composites with a single carbon layer are more likely to collapse during deep cycling, resulting in a rapid capacity loss.⁴⁵ Therefore, the double

carbon layer can not only block the direct contact between SnS particles and electrolyte, but also inhibits the volume expansion of SnS particles in the lithiation/delithiation process. The dual functions of packaging tin based sulfide volume change and stabilizing the SEI layer are realized by using double carbon layers in the cycle,⁴⁶ so that the coulomb efficiency, cycling stability and magnification performance of the N-DCSN electrode are greatly improved.

Electrochemical impedance spectroscopy (EIS) measurement can further explore the reaction mechanism of N-DCSN electrodes. Fig. 5a–b show the Nyquist diagram of bare SnS, CN/SnS and N-DCSN electrodes before the first charge/discharge and after 50 cycles at 0.2 A g⁻¹ current density. In addition, the equivalent circuit model is also shown in Fig. S10, ESI.† The semicircle in the high frequency region of the Nyquist diagram is attributed to the surface film resistance (R_f) and the interfacial charge transfer resistance (R_{ct}), while the slant in the low frequency region is attributed to the diffusion of Li⁺ in the active material.⁴⁷ In the high frequency region of Fig. 5a, the semicircle diameter of the N-DCSN electrode is smaller than that of the bare SnS and CN/SnS electrode, indicating that the conductivity of the N-DCSN electrode is the largest among the three. The conclusion can also be drawn by comparing the R_{ct} parameters of the N-DCSN electrode (24.24 Ω), CN/SnS electrode (57.19 Ω) and bare SnS electrode (61.77 Ω). Moreover, Fig. 5b reveals that the semicircle diameter of the N-DCSN electrode decreases significantly after 50 cycles, indicating that its conductivity increases further, which will help to enhance the stability of the interface between the electrode and

electrolyte.⁴⁸ Fig. 5d and e show the Z_{re} and $\omega^{-1/2}$ linear relationship of three electrode samples in the low frequency region, and it is fitted to Warburg factor σ_w . According to the Warburg factor (σ_w), the diffusion coefficient of the Li-ion (D value) can be directly determined, and the D value is negatively correlated with σ_w . The calculation formulas are as follows:⁴⁹

$$D = R^2 T^2 / 2 A^2 n^4 F^4 C^2 \sigma^2 \quad (1)$$

$$Z_{Re} = R_e + R_{ct} + \sigma \omega^{-1/2} \quad (2)$$

The relevant interpretation of the calculation formula is shown in the supporting literature (Depiction 1). The σ_w value of bare SnS before cycling (Fig. 5d) is the smallest, which can be attributed to the formation of a SEI film during the initial charge/discharge process of N-DCSN electrodes. Meanwhile, the comparison of discharge specific capacity in the first few cycles of the long-term cycling performance diagram (Fig. 4d) can also confirm this fact. Fig. 5e illustrates that the σ_w value of the N-DCSN electrodes changes slightly after 50 cycles. However, the σ_w values of bare SnS and CN/SnS electrodes increase significantly, indicating that the structure of electrodes collapses due to large volume strain. This fact can be attributed to the PANI carbon layer cutting off the direct contact between the electrode and the electrolyte, preventing side reactions and restraining electrolyte decomposition.⁴⁷ It also shows that the limiting effect of the double carbon layer packaging structure prevents the electrode structure from being greatly affected after a long-term charge/discharge process, and

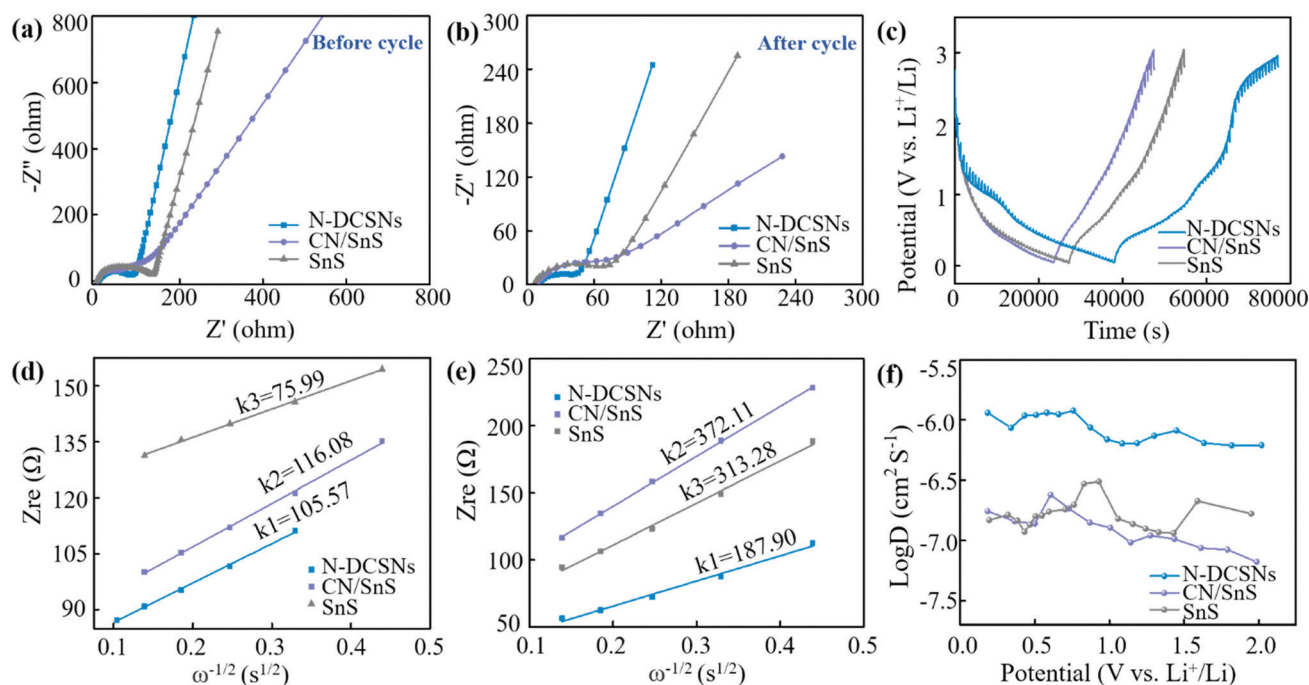


Fig. 5 Nyquist plots of bare SnS, CN/SnS and N-DCSN electrodes measured in the frequency region of 10^5 – 10^{-2} Hz before cycles (a) and after 50 cycles at 0.2 A g⁻¹ (b). The real part of the complex impedance versus $\omega^{-1/2}$ at open circuit voltage for bare SnS, CN/SnS and N-DCSN electrodes before cycles (d) and after 50 cycles (e), respectively. (c) The GITT curves of bare SnS, CN/SnS and N-DCSN electrodes under different discharge degrees. (f) Li-ion diffusion coefficient diagram at different discharge states.

still maintains a considerable Li-ion diffusion coefficient. The SEM images of the N-DCSN electrodes after rate performance and long-term cycles at 0.2 A g^{-1} proved this conjecture, as displayed in the ESI† (Fig. S11). The SEM image after 60 cycles showed that the morphology of N-DCSN electrodes did not change significantly. Even after 270 cycles, the structure remains remarkably intact, which is due to the synergistic protective effect of the double carbon layer. It is further confirmed that the excellent rate performance and long-term stability of N-DCSN electrodes are related to the special structure of the materials.

Galvanostatic intermittent titration (GITT) is a commonly used method to study the diffusion mechanism of solid ions, which is also used to measure the diffusion rate of Li^+ in electrode films. The electrodes of the three materials were fully discharged at a current density of 200 mA g^{-1} , then partially discharged at a current density of 100 mA g^{-1} , and then open circuit relaxation was observed for 10 minutes for GITT measurement. The GITT curves of bare SnS, CN/SnS and N-DCSN electrodes are shown in Fig. 5c. The chemical diffusion coefficients of the three materials in LIBs are determined by formulas 3 and 4 (Depiction S2):

$$D = \frac{4}{\pi} \left(\frac{I_0 V_M}{S F z_i} \right)^2 \left[\frac{dE}{d\delta} / \frac{dE}{d\sqrt{\tau}} \right]^2 \left(\tau \ll \frac{L^2}{D} \right) \quad (3)$$

$$D = \frac{4}{\pi \tau} \left(\frac{m_B V_M}{S M_B} \right)^2 \left(\frac{\Delta E_s}{\Delta E_\tau} \right)^2 \left(\tau \ll \frac{L^2}{D} \right) \quad (4)$$

Fig. 5f illustrates the Li^+ diffusion coefficient of the bare SnS, CN/SnS and N-DCSN electrodes during lithium intercalation. From 0.01 V to about 0.54 V, the GITT curve is downward, and the diffusion coefficient decreases. This can be attributed to the formation of a solid electrolyte interface (SEI) film at the electrode, which limits the diffusion of Li-ion. Then, due to the multi-step dealloying reaction, the diffusion rate is accelerated, corresponding to 0.68 V. Due to the conversion reaction of SnS ($\text{SnS} + 2\text{Li}^+ + 2\text{e}^- \rightarrow \text{Sn} + \text{Li}_2\text{S}$), the consumption of Li-ion is large, diffusion slows down, and the diffusion coefficient is the lowest at about 1.11 V. Finally, the diffusion rate is accelerated due to reversible transformation. The model shown in Fig. 6 illustrates the lithiation process, which is in accordance with the CV curve (Fig. 4a). During the lithiation process, Li^+ will insert into SnS interlayers, causing crystal structure expansion. The hexagonal SnS will be transformed into face-centered tetragonal $2\beta\text{-Sn}$ and cubic Li_2S by conversion reaction. After that, the orthogonal Li_xSn nanocrystals are formed by the alloying reaction. Furthermore, Li^+ and SnS can be reconverted by dealloying and conversion reaction during the process of delithiation. In the whole process, the Li-intercalation barrier is

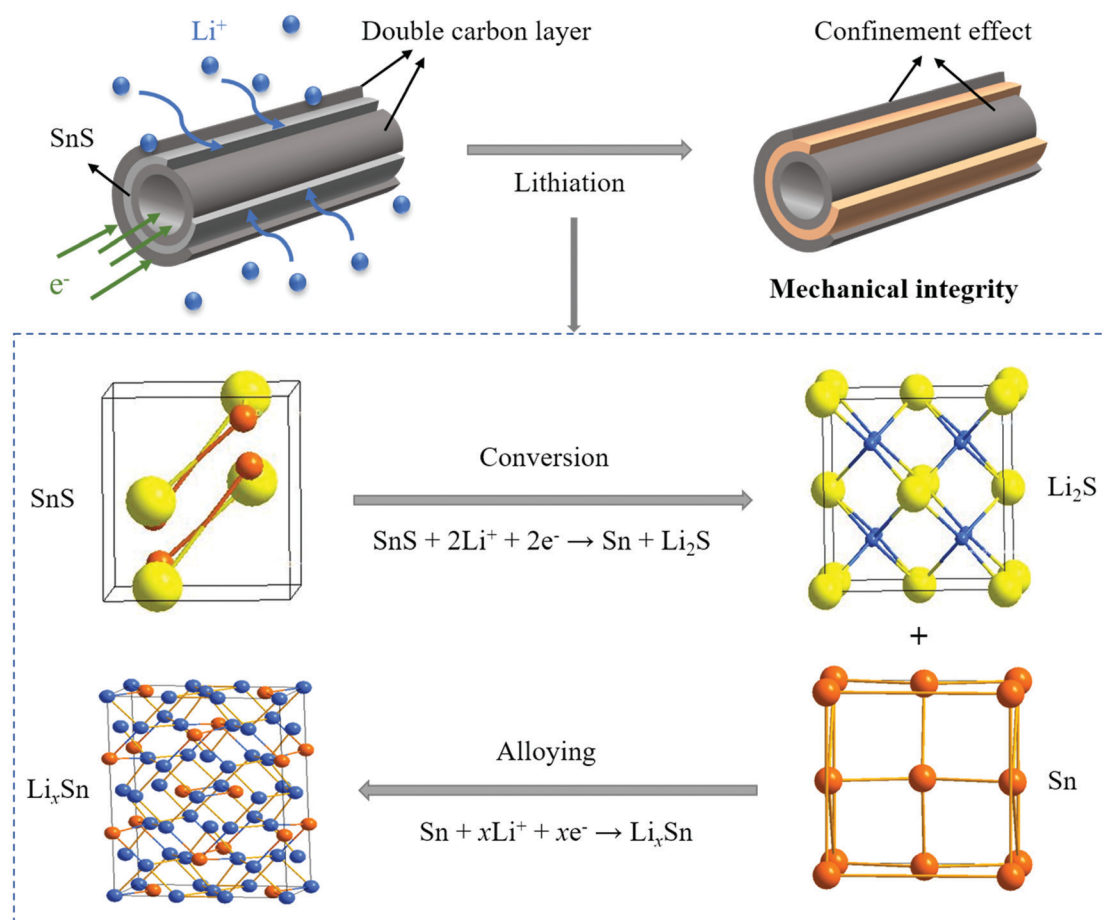


Fig. 6 Schematic representation of the initial lithiation mode of the electrodes.



reduced by the N-doped carbon matrix, making the lithiation/delithiation process reversible. In addition, strain of the crystal structure can be effectively relieved by the protection mechanism of the double carbon layer. Comparing the calculation results of the three materials, it can be seen that the average D_{Li} value range of bare SnS and CN/SnS electrodes is about $10^{-7} \text{ cm}^2 \text{ s}^{-1}$ in the voltage range of 2.1–0.01 V. The D_{Li} value of N-DCSN electrodes increases from 10^{-7} to $10^{-6} \text{ cm}^2 \text{ s}^{-1}$, showing the highest Li^+ diffusion coefficient. The result reasonably confirms that the special N-doped double carbon layer structure of N-DCSN electrodes can successfully improve the wettability of the organic electrolyte on carbon materials, and provide a two-way ion/electron transport channel between the inner and outer layers.²⁰ As a result, it becomes conducive to the diffusion of Li-ion through the interface between the carbon electrode and electrolyte, speeding up the diffusion rate.

4. Conclusions

In summary, a unique structure of SnS nanotube composites modified by the N-doped double carbon layer (N-DCSNs) is reported as the anode material for LIBs. The N-doped carbon matrix has high electronic conductivity and can effectually accelerate the kinetic rate of the electrode reaction. The volume strain of SnS can be successfully buffered by the synergistic effects of double carbon layer protective mechanism, which leads to satisfactory anode materials with high capacity and long-term cycling life. As a remarkable anode for LIBs, the N-DCSN electrode can obtain high capacities of 911.5 and 511.3 mA h g^{-1} at 0.2 and 1.0 A g^{-1} after 270 and 1000 cycles, respectively. The structural design is feasible and versatile, which provides direct experimental evidence for researching and designing high performance electrode materials.

Conflicts of interest

There are no conflicts to declare.

Acknowledgements

This work was financially supported by the National Natural Science Foundation of China (No. 52171207, 51772092, 51804116, and 51972109), the Hunan Provincial Natural Science Foundation of China (No. 2018JJ3207, 2017JJ2103, 2019JJ40102, and 2019JJ50205), the China Scholarship Council, the Scientific Research Fund of Hunan Provincial Education Department, China (No. 18B346, 18A315, 21B0604 and 18B347), the Scientific and Technological Project of Yueyang City and the Science Foundation of Educational Commission of Hubei Province of China (No. T2020008).

References

- Q. Wang, L. Jiang and Y. Yu, *et al.*, Progress of enhancing the safety of lithium ion battery from the electrolyte aspect, *Nano Energy*, 2019, 55, 93–114.
- H.-Q. Qu, H. Yin and Y.-L. Wang, *et al.*, Vapor selenization produced Bi_2Se_3 nanoparticles in carbon fiber 3D network as binder-free anode for flexible lithium-ion batteries, *Mater. Chem. Front.*, 2021, 5, 2832–2841.
- M. Jing, M. Zhou and G. Li, *et al.*, Graphene-embedded Co_3O_4 rose-spheres for enhanced performance in lithium ion batteries, *ACS Appl. Mater. Interfaces*, 2017, 9, 9662–9668.
- K. Liu, Y. Liu and D. Lin, *et al.*, Materials for lithium-ion battery safety, *Sci. Adv.*, 2018, 4, 9820.
- J. Lach, K. Wróbel and J. Wróbel, *et al.*, Applications of carbon in lead-acid batteries: a review, *J. Solid State Electrochem.*, 2019, 23, 693–705.
- H. Yin, K. S. Hui and X. Zhao, *et al.*, Eco-friendly synthesis of self-supported N-doped Sb_2S_3 -carbon fibers with high atom utilization and zero discharge for commercial full lithium-ion batteries, *ACS Appl. Energy Mater.*, 2020, 3, 6897–6906.
- A. Jin, N. Kang and J. H. Um, *et al.*, Sn(salen)-derived SnS nanoparticles embedded in N-doped carbon for high performance lithium-ion battery anodes, *Chem. Commun.*, 2020, 56, 8095–8098.
- P. He, Y. Fang and X. Y. Yu, *et al.*, Hierarchical nanotubes constructed by carbon-coated ultrathin SnS nanosheets for fast capacitive sodium storage, *Angew. Chem., Int. Ed.*, 2017, 56, 12202–12205.
- B. Zhao, D. Song and Y. Ding, *et al.*, Ultrastable Li-ion battery anodes by encapsulating SnS nanoparticles in sulfur-doped graphene bubble films, *Nanoscale*, 2020, 12, 3941–3949.
- Z. Hu, Q. Liu and S. L. Chou, *et al.*, Advances and challenges in metal sulfides/selenides for next-generation rechargeable sodium-ion batteries, *Adv. Mater.*, 2017, 29, 1700606.
- C. Zhu, P. Kopold and W. Li, *et al.*, A general strategy to fabricate carbon-coated 3D porous interconnected metal sulfides: case study of SnS/C nanocomposite for high-performance lithium and sodium ion batteries, *Adv. Sci.*, 2015, 2, 1500200.
- H.-J. Liang, Z.-Y. Gu and X.-Y. Zheng, *et al.*, Tempura-like carbon/carbon composite as advanced anode materials for K-ion batteries, *J. Energy Chem.*, 2021, 59, 589–598.
- D.-S. Liu, D.-H. Liu and B.-H. Hou, *et al.*, 1D porous $\text{MnO}@N$ -doped carbon nanotubes with improved Li-storage properties as advanced anode material for lithium-ion batteries, *Electrochim. Acta*, 2018, 264, 292–300.
- Z. Li, S. Xiao and J. Liu, *et al.*, Highly Efficient Na^+ Storage in Uniform Thorn Ball-Like $\alpha\text{-MnSe/C}$ Nanospheres, *Acta Metall. Sin-Engl.*, 2021, 34, 373–382.
- X. Yang, Y.-Y. Wang and B.-H. Hou, *et al.*, Nano-SnO₂ decorated carbon cloth as flexible, self-supporting and additive-free anode for sodium/lithium-ion batteries, *Acta Metall. Sin-Engl.*, 2021, 34, 390–400.
- J. Xia, L. Liu and S. Jamil, *et al.*, Free-standing SnS/C nanofiber anodes for ultralong cycle-life lithium-ion batteries and sodium-ion batteries, *Energy Storage Mater.*, 2019, 17, 1–11.
- S. Wang, Y. Fang and X. Wang, *et al.*, Hierarchical microboxes constructed by SnS nanoplates coated with nitrogen-doped



- carbon for efficient sodium storage, *Angew. Chem., Int. Ed.*, 2019, **58**, 760–763.
- 18 M. Jing, Z. Chen and Z. Li, *et al.*, Facile synthesis of ZnS/N,S Co-doped carbon composite from zinc metal complex for high-performance sodium-ion batteries, *ACS Appl. Mater. Interfaces*, 2018, **10**, 704–712.
 - 19 X. Zhong, Y. Wu and S. Zeng, *et al.*, Carbon and Carbon Hybrid Materials as Anodes for Sodium-Ion Batteries, *Chem. – Asian J.*, 2018, **13**, 1248–1265.
 - 20 Z.-S. Wu, W. Ren and L. Xu, *et al.*, Doped graphene sheets as anode materials with superhigh rate and large capacity for lithium ion batteries, *ACS Nano*, 2011, **5**, 5463–5471.
 - 21 Y. Xu, Y. Zhou and J. Guo, *et al.*, Preparation of SnS₂/g-C₃N₄ composite as the electrode material for Supercapacitor, *J. Alloys Compd.*, 2019, **806**, 343–349.
 - 22 J. Fu, J. Yu and C. Jiang, *et al.*, G-C₃N₄-based heterostructured photocatalysts, *Adv. Energy Mater.*, 2018, **8**, 1701503.
 - 23 G. M. Weng, Y. Xie and H. Wang, *et al.*, A promising carbon/g-C₃N₄ composite negative electrode for a long-life sodium-ion battery, *Angew. Chem., Int. Ed.*, 2019, **131**, 13865–13871.
 - 24 M. Zhou, Z. Hou and L. Zhang, *et al.*, n/n junctioned g-C₃N₄ for enhanced photocatalytic H₂ generation, *Sustainable Energy Fuels*, 2017, **1**, 317–323.
 - 25 W. Hu, L. Chen and M. Du, *et al.*, Hierarchical NiCo-layered double hydroxide nanoscroll@PANI nanocomposite for high performance battery-type supercapacitor, *Electrochim. Acta*, 2020, **338**, 135869.
 - 26 Z. Chen, Z. Hou and W. Xu, *et al.*, Ultrafine CuO nanoparticles decorated activated tube-like carbon as advanced anode for lithium-ion batteries, *Electrochim. Acta*, 2019, **296**, 206–213.
 - 27 N. Venkatesan, K. S. Archana and S. Suresh, *et al.*, Boron-doped graphene as efficient electrocatalyst for zinc-bromine redox flow batteries, *ChemElectroChem*, 2019, **6**, 1107–1114.
 - 28 J. Liu, M. Gu and L. Ouyang, *et al.*, Sandwich-like SnS/Polypyrrole ultrathin nanosheets as high-performance anode materials for Li-ion batteries, *ACS Appl. Mater. Interfaces*, 2016, **8**, 8502–8510.
 - 29 C. Yu and X.-X. Yu, *et al.*, Piezoelectric potential enhanced photocatalytic performance based on ZnO with different nanostructures., *Nanotechnology*, 2021, **32**(13), 135703.
 - 30 H. Hou, X. Qiu and W. Wei, *et al.*, Carbon anode materials for advanced sodium-ion batteries, *Adv. Energy Mater.*, 2017, **7**, 1602898.
 - 31 H. Wang, K. Dou and W. Teoh, *et al.*, Engineering of facets, band structure, and gas-sensing properties of hierarchical Sn²⁺-doped SnO₂ Nanostructures, *Adv. Funct. Mater.*, 2013, **23**, 201300303.
 - 32 D. Xiong, Q. Zhang and W. Li, *et al.*, Atomic-layer-deposited ultrafine MoS₂ nanocrystals on cobalt foam for efficient and stable electrochemical oxygen evolution, *Nanoscale*, 2017, **9**, 2711–2717.
 - 33 Z. Wang, Y. Dong and H. Li, *et al.*, Enhancing lithium-sulphur battery performance by strongly binding the discharge products on amino-functionalized reduced graphene oxide, *Nat. Commun.*, 2014, **5**, 5002.
 - 34 W. Li, M. Zhou and H. Li, *et al.*, A high performance sulfur-doped disordered carbon anode for sodium ion batteries, *Energy Environ. Sci.*, 2015, **8**, 2916–2921.
 - 35 X. Zhou, L. J. Wan and Y. G. Guo, Binding SnO₂ nanocrystals in nitrogen-doped graphene sheets as anode materials for lithium-ion batteries, *Adv. Mater.*, 2013, **25**, 2152–2157.
 - 36 Z. Lin, G. Waller and Y. Liu, *et al.*, Facile synthesis of nitrogen-doped graphene via pyrolysis of graphene oxide and urea, and its electrocatalytic activity toward the oxygen-reduction reaction, *Adv. Energy Mater.*, 2012, **2**, 884–888.
 - 37 Q. Lin, J. Zhang and W. Lv, *et al.*, A functionalized carbon surface for high-performance sodium-ion storage, *Small*, 2020, **16**, 1902603.
 - 38 L. Yao, M. Nie and C. Zhu, *et al.*, Revealing a conversion-alloying reaction mechanism behind high capacity and rate capability of SnS/N-doped graphene anode by in situ TEM, *Electrochim. Acta*, 2019, **297**, 46–54.
 - 39 J. Cai, Z. Li and P. K. Shen, Porous SnS nanorods/carbon hybrid materials as highly stable and high capacity anode for Li-ion batteries, *ACS Appl. Mater. Interfaces*, 2012, **4**, 4093–4098.
 - 40 W. Ai, Z. Huang and L. Wu, *et al.*, High-rate, long cycle-life Li-ion battery anodes enabled by ultrasmall tin-based nanoparticles encapsulation, *Energy Storage Mater.*, 2018, **14**, 169–178.
 - 41 Z. Deng, H. Jiang and Y. Hu, *et al.*, Nanospace-confined synthesis of coconut-like SnS/C nanospheres for high-rate and stable lithium-ion batteries, *AIChE J.*, 2018, **64**, 1965–1974.
 - 42 Y. Chen, Q. Wu and Y. Song, Magnetic recyclable lanthanum-nitrogen co-doped titania/strontium ferrite/diatomite heterojunction composite for enhanced visible-light-driven photocatalytic activity and recyclability, *Chem. Eng. J.*, 2019, **373**, 192–202.
 - 43 J. Liu, Y. Wen and P. A. van Aken, *et al.*, In situ reduction and coating of SnS₂ nanobelts for free-standing SnS@polypyrrole-nanobelt/carbon-nanotube paper electrodes with superior Li-ion storage, *J. Mater. Chem. A*, 2015, **3**, 5259–5265.
 - 44 S. Zhu and H. Yin, *et al.*, Heteroatomic interface engineering of MOF-derived metal-embedded P and N-codoped Zn node porous polyhedral carbon with enhanced sodium-ion storage., *ACS Appl. Energy Mater.*, 2020, **3**(9), 8892–8902.
 - 45 L. Hu, B. Luo and C. Wu, *et al.*, Yolk-shell Si/C composites with multiple Si nanoparticles encapsulated into double carbon shells as lithium-ion battery anodes, *J. Energy Chem.*, 2019, **32**, 124–130.
 - 46 C.-Z. Yuan and K. S. Hui, *et al.*, Regulating Intrinsic Electronic Structures of Transition-Metal-Based Catalysts and the Potential Applications for Electrocatalytic Water Splitting, *ACS, Mater. Lett.*, 2021, **3**, 752–780.



- 47 H. Yin, W. Shen and H.-Q. Qu, *et al.*, Boosted charge transfer and Na-ion diffusion in cooling-fins-like Sb_2Te -Te nano-heterostructure for long cycle life and high rate capability anode, *Nano Energy*, 2020, **70**, 104468.
- 48 J.-M. Jeong, K. G. Lee and S.-J. Chang, *et al.*, Ultrathin sandwich-like MoS_2 @N-doped carbon nanosheets for anodes of lithium ion batteries, *Nanoscale*, 2015, **1**, 324–329.
- 49 H. Yin, X.-X. Yu and H. Zhao, *et al.*, Towards high-performance cathode materials for lithium-ion batteries: Al_2O_3 -coated $\text{LiNi}_{0.8}\text{Co}_{0.15}\text{Zn}_{0.05}\text{O}_2$, *J. Solid. State. Electr.*, 2018, **22**, 2395–2403.

